nanomaterials

MDPI

Article

Impact of Ar Flow Rates on Micro-Structural Properties of WS_2 Thin Film by RF Magnetron Sputtering

Md. Akhtaruzzaman [1], Md. Shahiduzzaman [2,*], Nowshad Amin [3,*], Ghulam Muhammad [4], Mohammad Aminul Islam [5], Khan Sobayel Bin Rafiq [1,*] and Kamaruzzaman Sopian [1]

1 Solar Energy Research Institute, The National University of Malaysia, Bangi 43600, Malaysia; akhtar@ukm.edu.my (M.A.); ksopian@ukm.edu.my (K.S.)
2 Graduate School of Natural Science and Technology, Kanazawa University, Kakuma, Kanazawa 920-1292, Japan
3 Institute of Sustainable Energy, Universiti Tenaga Nasional (@The National Energy University), Jalan Ikram-Uniten, Kajang 43000, Malaysia
4 Department of Computer Engineering, College of Computer and Information Sciences, King Saud University, Riyadh 11451, Saudi Arabia; ghulam@ksu.edu.sa
5 Department of Electrical Engineering, University of Malaya, Jalan Universiti, Kuala Lumpur 50603, Malaysia; aminul.islam@um.edu.my
* Correspondence: shahiduzzaman@se.kanazawa-u.ac.jp (M.S.); nowshad@uniten.edu.my (N.A.); sobayel@ukm.edu.my (K.S.B.R.)

Abstract: Tungsten disulfide (WS_2) thin films were deposited on soda-lime glass (SLG) substrates using radio frequency (RF) magnetron sputtering at different Ar flow rates (3 to 7 sccm). The effect of Ar flow rates on the structural, morphology, and electrical properties of the WS_2 thin films was investigated thoroughly. Structural analysis exhibited that all the as-grown films showed the highest peak at (101) plane corresponds to rhombohedral phase. The crystalline size of the film ranged from 11.2 to 35.6 nm, while dislocation density ranged from 7.8×10^{14} to 26.29×10^{15} lines/m^2. All these findings indicate that as-grown WS_2 films are induced with various degrees of defects, which were visible in the FESEM images. FESEM images also identified the distorted crystallographic structure for all the films except the film deposited at 5 sccm of Ar gas flow rate. EDX analysis found that all the films were having a sulfur deficit and suggested that WS_2 thin film bears edge defects in its structure. Further, electrical analysis confirms that tailoring of structural defects in WS_2 thin film can be possible by the varying Ar gas flow rates. All these findings articulate that Ar gas flow rate is one of the important process parameters in RF magnetron sputtering that could affect the morphology, electrical properties, and structural properties of WS_2 thin film. Finally, the simulation study validates the experimental results and encourages the use of WS_2 as a buffer layer of CdTe-based solar cells.

Keywords: tungsten disulfide (WS_2); thin film; radio frequency magnetron sputtering; gas flow rate; defect engineering

Citation: Akhtaruzzaman, M..; Shahiduzzaman, M..; Amin, N.; Muhammad, G.; Islam, M.A.; Rafiq, K.S.B.; Sopian, K. Impact of Ar Flow Rates on Micro-Structural Properties of WS_2 Thin Film by RF Magnetron Sputtering. *Nanomaterials* **2021**, *11*, 1635. https://doi.org/10.3390/nano11071635

Academic Editor: Christophe Detavernier

Received: 30 May 2021
Accepted: 16 June 2021
Published: 22 June 2021

1. Introduction

Historically, chalcogenides of the first-row transition materials have drawn researchers' interest for their elementary abundance and impressive structural characteristics [1]. The characteristic features of these chalcogenides are their well-known two-dimensional structures in which metal and chalcogen are periodically arranged. Transition-metal dichalcogenides (TMDCs) are commonly known as 2D materials that exhibit hexagonal structure, but their hexagonal structure is not atomic-thin like graphene. The overall efficiency of atomically thin TMDCs based devices depends on a number of factors, including stability, thickness, substratum, contacts, temperature, and surface functionalization of material. Few-layered MX_2 (M = Mo, W; X = S, Se) TMDCs exhibit various fascinating properties associated with their reduced thickness [2,3]. For example, TMDCs undergo a layer-dependent transition in their band structure from an indirect to a direct bandgap

semiconductor [4,5]. This transition immediately makes TMDCs attractive for electronics and optoelectronics applications [2,6]. TMDC-based instruments, however, exhibit n- or p-type behavior, contradicting what one would expect from a perfect crystal structure without unsaturated bonds [7].

TMDCs may contain a variety of structural defects in their crystal labels that alter their physicochemical properties significantly. Such observations point to a simple fact: structural defects in TMDCs cannot simply be ignored [8,9]. Tungsten disulfide (WS_2) exhibits a sandwich-type basic building block structure composed of a sheet of hexagonal close-packed transition-metal atoms between two sheets of hexagonal close-packed chalcogen atoms. Atoms within a sheet are bonded by covalent bonds, whereas the individual sheets are stacked by weaker van der Waals (vdW) bonds. Due to weaker vdW bonds in the latter one, this structure becomes sensitive to any small changes of growth parameter resulting in various types of defects such as stacking defect, edge defect, line defect, etc. [10–14]. Moreover, a small modification of the synthesis path also leads to significant variations in the electronic properties of the material [15]. Based on the intend of application, structural defects can be counterproductive or beneficial [8,16,17], but mostly it has a detrimental effect. In the case of photovoltaic applications, structural defects are mostly harmful. Defects positioned either in the interface of the absorber and window layer or within the absorber layer always hinder the overall performance of solar cells [18]. Realistic incorporation of TMDCs into devices is far from optimal standard. The existence of structural defects in TMDCs is the main bottleneck for which TMDCs are prevented from being integrated into modern devices [19]. Therefore, a comprehensive understanding of structural defects and defect engineering is required.

Radiofrequency (RF) magnetron sputtering is a plasma or ion-assisted deposition process commonly used for the fabrication of thin film due to its high yield rate and ability to produce uniformity on the film [20]. Increasing the working gas flow rate is highly suspected to result in an increase in energy flux at the substrate that can lead to a higher deposition rate and bigger grain growth. Again, with higher gas flow rate and moderately high power leads to a high bombardment of the atom, which may cause sputter damage to the film. Hence, optimization of gas flow rate is necessary to achieve desired material properties [21,22]. Many experimental works have been undertaken to study the effect of process parameters of RF magnetron sputtering on thin film properties. The type of gas and variations in flow rate during sputtering has an enormous effect on thin film properties [23–26]. Usually, the gas flow rate directly influences the sputtering yield. The energy and energy distribution of sputtered atoms varies with the change of gas flow rate, which influences morphological and electrical properties of the thin film [24,27]. As Ar facilitates to achieve plasma from the source material without taking part in any reaction, it is commonly used for sputtering. Moreover, the gas flow rate has a significant influence on film stoichiometry, phase composition, and preferred orientation as well [28–32]. It is also reported that argon-nitrogen gas mixtures influence the structural properties of the film and improve the adhesivity [33]. However, there have not been many attempts to examine the impact of Ar gas flow rate on the WS_2 thin film properties. This study is a follow-up work of previously reported studies on WS_2 thin film [22,23] and devoted to investigating the impact of variation in gas flow rate on the WS_2 film properties in order to achieve higher crystallite, defect-free, uniform film for the application in the solar cell. As a whole, the objective of this study is to evaluate the micro-structural changes of WS_2 thin film that occurred due to the variation in gas flow rate.

2. Materials and Methods

In this study, WS_2 thin film was deposited for 30 min on soda-lime glass substrates of 7.5 cm × 2.5 cm × 0.2 cm by RF magnetron sputtering technique. Substrates were cleaned prior to deposition following the sequential cleaning process, such as mechanical scrubbing followed by acetone-methanol-deionized water in ultrasonic bath and later dried with N_2 gas flow. A 50 mm diameter WS_2 (99.99%) sputtering target (supplied by Kurt.

J. Lesker, USA) was used as the source material. Purging of the sputtering chamber was carried out thrice to remove unwanted particles from the chamber. Afterward, the chamber pressure was brought down to 10^{-6} torr by the turbo-molecular pump. Working pressure ranges from 1.3 to 1.8 Pa with the variation of gas flow rate throughout the deposition process. and substrate temperature was fixed at 100 °C during the deposition. Substrate-to-target distance (sputter up) and substrate holder rotation were fixed at 8 cm and 10 rpm, respectively. In this experiment, Ar gas flow rate was varied from 3 to 7 sccm to identify its impact on the crystallite structure of WS_2 thin film. To avoid the significant contamination of film by oxygen or hydrogen from the residual atmosphere, initially purging was carried out to the chamber, and later substrates had been preheated by 100 °C for 15 min before deposition. Schematic of sputtering is shown in Figure 1. Deposition parameters used for this study are shown in Table 1. All the samples were kept inside the sputtering chamber upon completion of the deposition until substrate temperature falls to room temperature as a measure to prevent as-grown films from being oxidized.

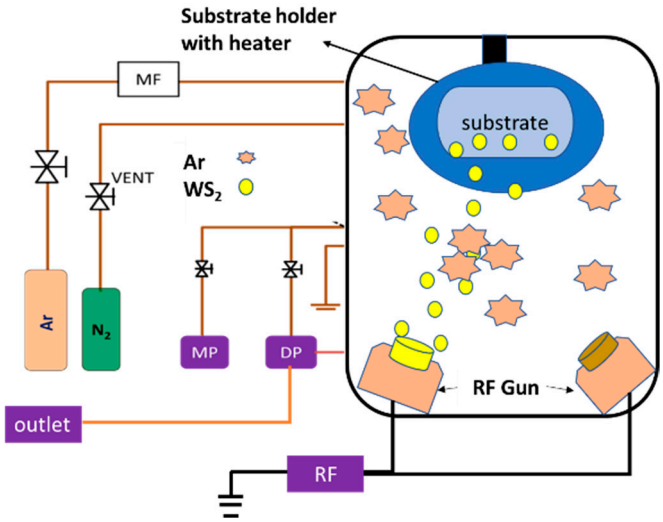

Figure 1. Schematic diagram of RF magnetron sputtering system.

Table 1. WS_2 fabrication parameters.

Parameters	WS_2 Fabrication Process
Preheat temperature	100 °C
Preheat time	15 min
Growth temperature	100 °C
RF power	50 W
Ar gas flow	3, 4, 5, 6, 7 sccm
Base pressure	10^{-6} Torr
Operating pressure	1.3~1.8 Pa
Deposition time	30 min

A BRUKER aXS-D8 Advance CuKα diffractometer (USA) was used to characterize the structural and crystalline properties of the as-grown films. X-ray diffraction (XRD) patterns were recorded in the 2θ range of 10° to 80° with a step size of 0.05° using Cu Kα radiation wavelength, λ = 0.15408 nm. Surface morphology and cross-sectional view of the films were observed by using FEI Quanta 400F (USGS, USA) field emission scanning electron microscope (FESEM) at 10 kV operating voltage. The atomic composition was determined by Horiba EMAX 450 (Horiba, UK) energy-dispersive X-ray spectroscopy (EDX). This method provided the atomic percentage (at %) of W and S atoms present in the sample. The electronic properties of the films were measured by the HMS ECOPIA 3000 Hall Effect

measurement system (Bridge Technology, USA) with a magnetic field of 0.57 T and probe current of 100 nA for all the samples. Pinholes were investigated by keeping as-deposited samples over a light source, and the adhesiveness of films was tested by the scotch-tape method.

3. Results and Discussions

3.1. Structural Analysis from XRD

The XRD analysis was performed to investigate the crystallographic properties of as-grown WS_2 thin film. Usually, a single layer of TMDC material forms an atomic tri-layer, which consists of two adjacent layers of chalcogen atoms (X) covalently bonded by a layer of transition-metal atoms (M), forming an X-M-X layer configuration. This structure corresponds to two possible structural polytypes: the semiconducting trigonal prismatic phase (1H or 2H phase) and the metallic octahedral prismatic phase (1T) [34–37]. Figure 2 represents the crystal phases and crystallinity of WS_2 films of different gas flow rates. It reveals that films deposited at different Ar flow rates exhibit two primary peaks of (101) and (112) orientations. All the films are found at the 3R phase and exhibit the most intense peak at $2\theta = 34.9°$, corresponding to (101) plane at 5 sccm gas flow rate. When TMDC crystals have more than one atomic sulfur-metal-sulfur layer of the 1H phase bonded by van der Waals (vdW) forces, additional polytypes appear in response to variations in stacking orders. This stacking order is known as Bernal stacking that portraits the rhombohedral phase denominated as the 3R phase. It is found that the XRD peak almost overlaps each other at a higher gas flow rate. Noteworthy that a slight peak shift has been observed for WS_2 films in this experiment, which may be due to expansion or compression of the lattice caused by stress. Finally, we can conclude that as-grown films are almost pure in nature and did not oxidize during the process of fabrication [38].

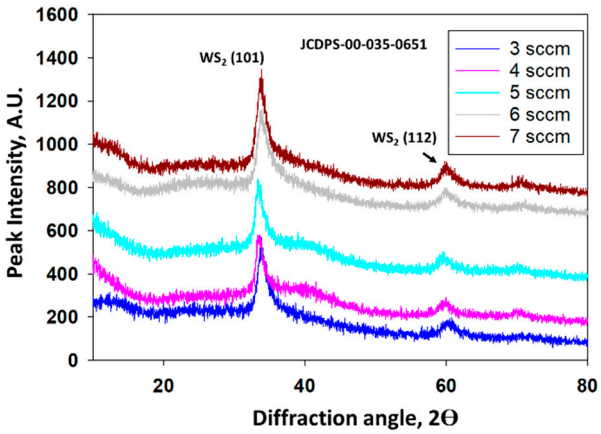

Figure 2. XRD patterns of WS_2 under different gas flow rates.

Peak width (β) is inversely proportional to crystallite size (L). In this study, the β value is almost the same for all variations. The details of the XRD analysis are given in Appendix A. The average particle size or crystallite size was calculated from the broadening of the (101) peak using the Scherrer equation [39].

$$L_{hkl} = 0.9\lambda/(\beta\cos\theta) \quad (1)$$

where L, λ, β, θ are the crystallite size, wavelength, β and θ is the angle between the incident and scattering planes, respectively. Figure 3a represents the crystallite size and growth rate of WS_2 at different Ar gas flow rates. The crystallite size of the film ranges from 35.3 to 44.8 nm and follows the same pattern with the growth rate. It has been observed that crystallite size increases initially with the increase in Ar gas flow rate but starts decreasing from 6 sccm of gas flow rate and found lowest at 7 sccm Ar flow rate.

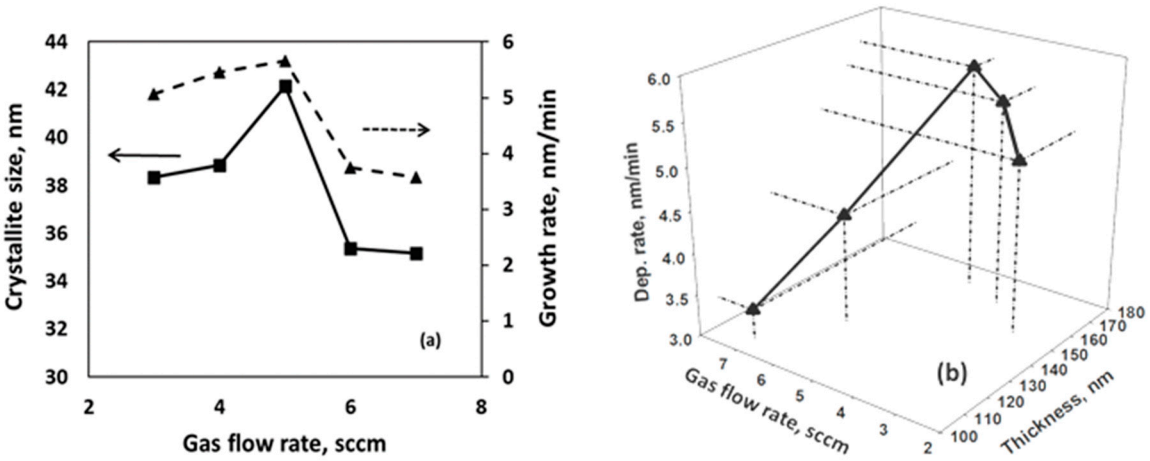

Figure 3. (**a**) Crystallite size and growth rate and (**b**) thickness and deposition rates of as-grown WS_2 under different Ar gas flow rates.

Figure 3b represents the film thickness (Table S1) and growth rate of WS_2 at different gas flow rates. It has been found that the growth rate increases initially with the increase in gas flow rate and decreases drastically when the gas flow rate increases from 5 sccm flow rate. The highest growth rate has been obtained at 5.69 nm/min at 5 sccm Ar flow rate, and the lowest has been found at 3.37 nm/min at 7 sccm Ar flow rate.

3.2. Williamson–Hall (W-H) Analysis

Lattice strains can be developed in the films via scattered grains distribution and/or relocation of the atoms from their reference-lattice positions; however, these phenomena are in turn dependent on the films' predation conditions, including deposition parameters and sub-sequent annealing conditions. Simply, the lattice strain that developed in the film can be known by estimating "micro-strain". Scherrer equation neglects the importance of the micro strain (ε), whereas its effects remain present in the diffraction pattern, as this intrinsic strain also produces the broadening in the X-ray profile [40,41]. The contribution of the micro strain to the line broadening of the diffraction peak is defined by Stokes and Wilson and can be calculated as:

$$\beta_\varepsilon = 4\varepsilon \tan\theta \quad (2)$$

The Williamson–Hall equation varies with tan θ only, whereas the Debye–Scherrer equation follows 1/cos θ [42,43]. The addition of Equations (1) and (2) gives the observed broadening (βhkl) assuming the contribution of particle size and strain:

$$\beta_{hkl} = \beta_L + \beta_\varepsilon \quad (3)$$

$$\beta_{hkl} = 0.9\lambda/L \cos\theta + 4\varepsilon \tan\theta \quad (4)$$

$$\beta_{hkl} \cos\theta = 0.9\lambda/L + 4\varepsilon \sin\theta \quad (5)$$

Williamson–Hall (W-H) plot of as-deposited WS_2 film at 5 sccm and 7 sccm Ar flow rates are represented in Figures 4 and 5, respectively. W-H plotting consists of a plot of $\beta_{hkl} \cos\theta$ versus sin θ, which becomes a straight line. The slope provides the value of micro strain, and the mean particle size can be obtained from the intercept. The highest strain was found 75.52×10^{-4} at 6 sccm Ar gas flow rate, while the lowest was observed at 5 sccm gas flow rate, which is 2.36×10^{-4}. The negative slope of strain that occurs due to the staking fault of atoms indicates the compressive strain [44]. The lower strain value denotes the larger crystallite size.

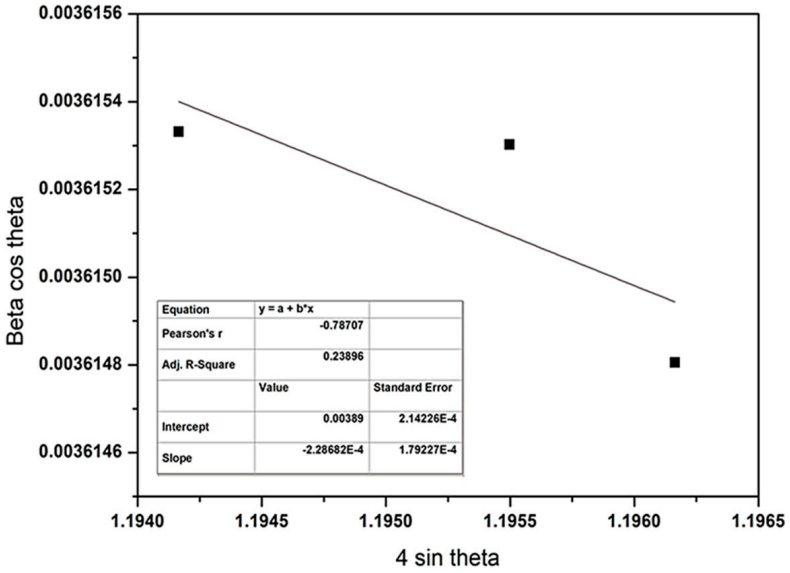

Figure 4. Williamson–Hall plot of as-deposited WS_2 film at 5 sccm of Ar flow rate.

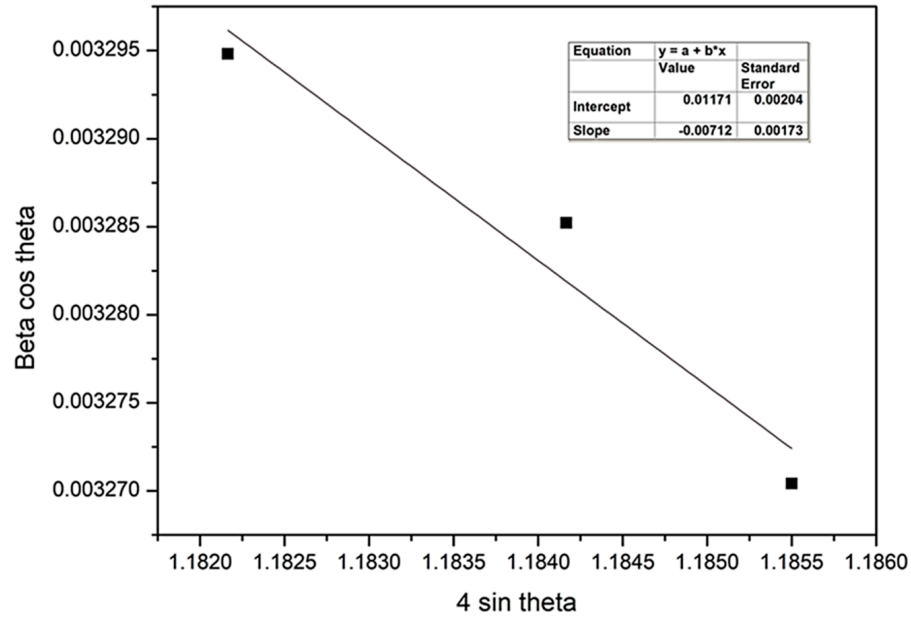

Figure 5. Williamson–Hall plot of as-deposited WS_2 film at 7 sccm of Ar flow rate.

Figure 6 represents the relationship between crystallite size and strain with respect to Ar flow rate and revealed that 5 sccm Ar flow rate provides a larger crystallite size and lowest strain value for WS_2 film. This phenomenon is completely in agreement with the literature as discussed above. Geometric parameters obtained from XRD are given in Appendix A (Table A1).

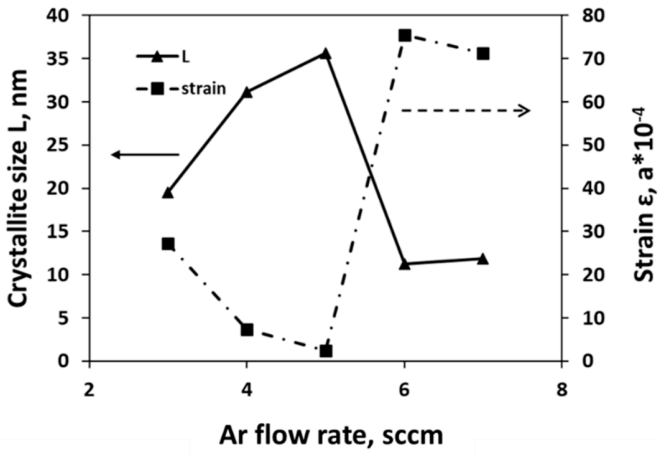

Figure 6. Relation between crystallite size (L) and strain for different gas flow rates of as-deposited WS_2 films.

3.3. Study on Structural Deformation and Defects

The lattice strains exhibit displacement of atoms from their original lattice positions. It may occur due to high energetic deposition. In addition, a lower value of strain signifies higher crystallinity [40]. Alternatively, the atoms that displace from its reference lattice could act as interstitial atoms and its reference place could act as an unlike vacancy in the crystals. The number of atoms that are displaced from their reference lattice could realize via estimating the dislocation density. Dislocation density can be determined by the following equation [44–48]:

$$\text{Dislocation density; } \delta = 1/L^2 \quad (6)$$

where L have their usual significances as mentioned above section. Strain and crystallite size (L) are inversely related. Dislocation density (δ) and crystallites per unit area are represented in Figure 7. It is noteworthy that dislocation density and crystallites per unit area follow the same trend. It is found that dislocation density suddenly rises sharply when films are deposited over 5 sccm Ar gas flow rate. It signifies that imperfections in the crystal lattice, commonly termed as defects that can be either point defect or line defect, increases at a higher Ar flow rate. Moreover, at higher gas flow rates, spikes (discussed in the later part) are being observed. Hence, it can be derived that variation in gas flow rate during RF magnetron sputtering may lead to imperfections in the crystal lattice by changing the crystallographic structure of WS_2 thin film.

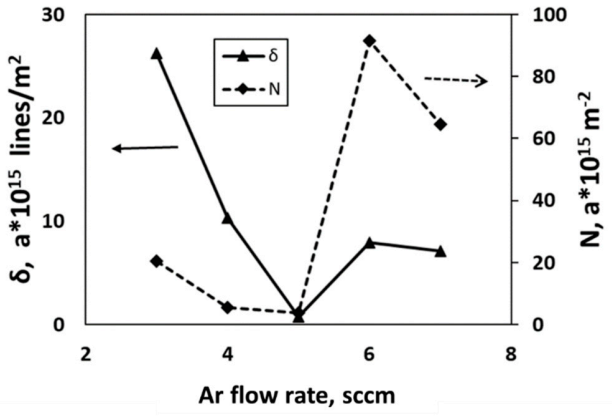

Figure 7. Relation between dislocation density (δ) and crystallites per unit area (N) for different Ar gas flow rates of as-deposited WS_2 films.

A perfect crystal (Figure 8i) contains the same lattice matrix that has the same unit cell throughout the crystal. The term imperfection or defect is generally used to describe any deviation of the ideally perfect crystal from the periodic arrangement of its constituents. TMDC materials mostly exhibit interface defects due to stacking fault or line defects [37]. Figure 8ii represents the schematic of the stacking defect, and Figure 8iii shows the schematic of the line defect, respectively. The adjacent layers in WS_2 are associated with the vdW forces. The intensity of vdW forces depends on the layer spacing, which is correlated to the configuration of the stacking. WS_2 is usually layered as Bernal stacking (AbAb), but deviations from the structure can also be made possible due to the process of synthesis. In contrast, the vacancies of sulfur in the WS_2 atomic structure forms lines defects, which usually been observed in PVD methods. It is reported that both single and double-line vacancies are observed experimentally for WS_2 [36,49,50].

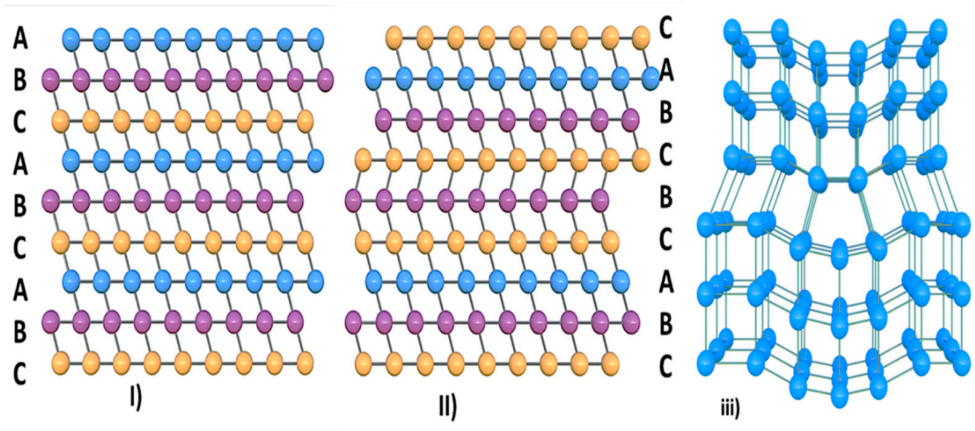

Figure 8. Schematic of defects in TMDC materials: (**i**) perfect crystal; (**ii**) stacking defect; and (**iii**) line defect.

3.4. Morphological Analysis

In the previous section, it was revealed that as-grown WS_2 thin films have defects at different scales at their respective crystallographic structure. For visualizing the presence of defects, we have further analyzed its morphological properties through FESEM images. Figure 9 shows the top view of deposited WS_2 films under different gas flow rates. All the films appear to be non-uniform and porous microstructures (Detail image in Figure S1). As-grown films show lamellar morphology for all the variations of gas flow rate, which is also supported by Regula et al. [50]. Interestingly, spikes are observed on the layered structure of WS_2. The reason for these spikes might be the stacking deformation or edge defect due to sulfur deficit. We also observe that the number of spikes gradually increases with the increase in gas flow rate.

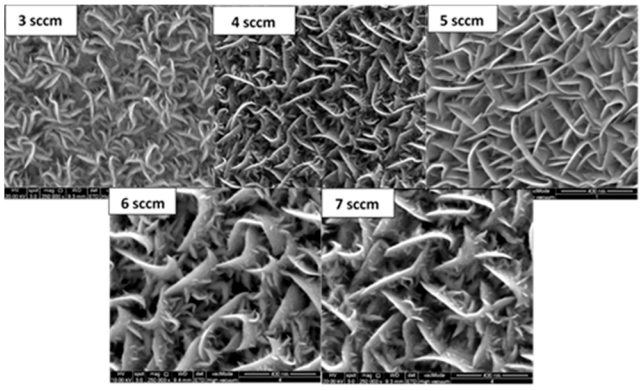

Figure 9. Top view of deposited WS_2 films under different gas flow rates.

The average size of observed spikes and grain size with respect to different gas flow rates have been measured by ImageJ software [51], as illustrated in Figure 10. No significant changes have been observed on the average grain size of as-deposited WS_2 film for different gas flow rates. However, it has been found that the length of spikes gradually decreases with the increase in gas flow rate and is smallest at 5 sccm Ar flow rate. Above 5 sccm gas flow rate, it starts to increase again. This might be due to the loss of S atoms during WS_2 deposition at higher gas flow rates or due to the sputtering damage of the film [26,52].

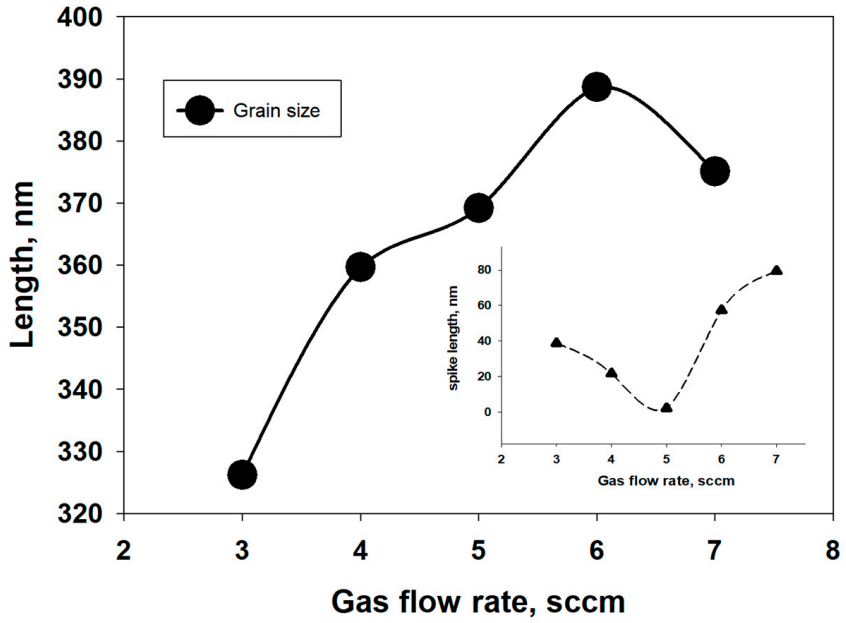

Figure 10. Spike and grain length vs. Ar gas flow rate.

Figure 11 depicts the highly magnified FESEM images of WS_2 thin film deposited on 5 sccm and 7 sccm of Ar gas flow rates. Very low crystallographic deformation has been observed at 5 sccm gas flow rate, and on the other hand, maximum deformation was found at 7 sccm gas flow rate. As at lower gas flow rate exhibits least crystallographic deformation; hence, it can be said that structural defects can be passivated for WS_2 thin film in PVD method by varying Ar flow rate. The mean free path of a sputtered atom is almost fixed for a system. Sputtered atoms have to go through a number of collisions before reaching the substrate. Increasing working gas flow rate is highly suspected to result in increased energy flux at the substrate surface, which can lead to a higher deposition rate [20]. Again, at a very high gas flow rate (more than an optimized one), the number of atomic collisions is more that results in the higher rate of scattering of sputtered atoms. Thus, too high a gas flow rate reduces the deposition rate and increases the penetration depth of an atom [53,54].

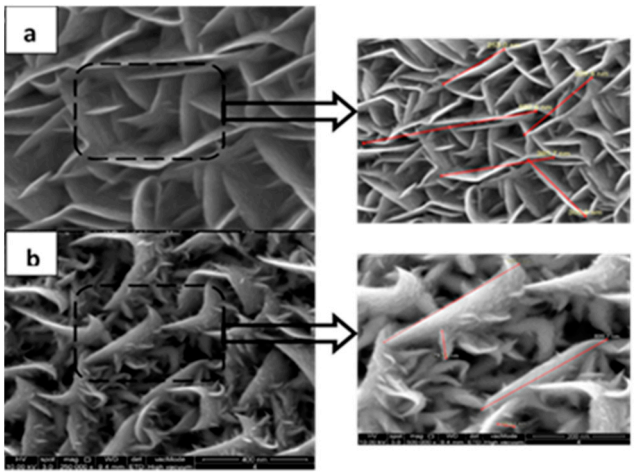

Figure 11. Highly magnified FESEM image of as-grown WS_2 at different gas flow rates (**a**) 5 sccm and (**b**) 7 sccm.

3.5. Compositional Analysis by EDX

To investigate and to reconfirm the type of defect of this experiment, we have conducted EDX analysis (Figure S2 in supplementary data) by using Area Scan Mode on the film surface. Figure 12 represents the S to W ratio for different Ar flow rates during WS_2 deposition. It reveals that atomic percentage (at %) of S increases with the increase in gas flow rate and is found highest at 5 sccm flow, which is 1.81:1, and lowest is observed at 6 sccm flow rate, which is 1.44:1. At a very higher gas flow rate, the atomic % of S is much less. It might be because of the scattering effect during deposition of the thin film at a higher gas flow rate. This phenomenon agrees with our findings in the structural properties.

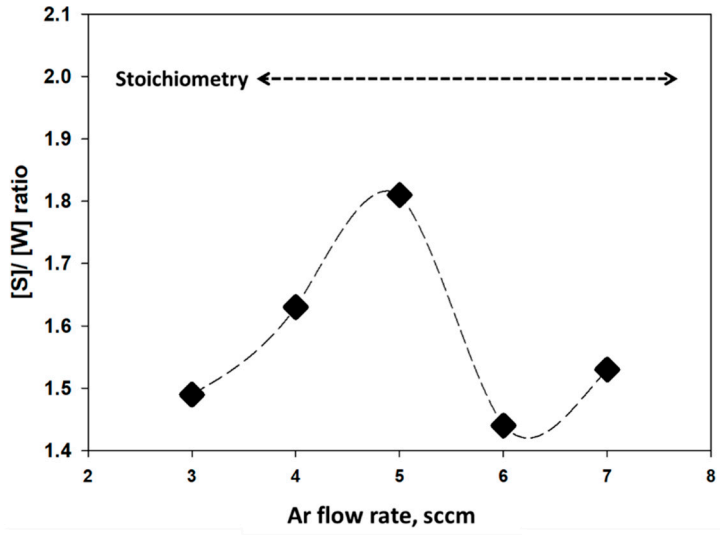

Figure 12. S/W ratio in as-grown WS_2 under different Ar gas flow rates.

To obtain the best properties from any compound, it is essential to achieve stoichiometry of that compound. From this experiment, it is found that all the as-grown WS_2 films by RF magneto sputtering are sulfur (S) deficit and far away from stoichiometry. Hence, we can conclude that the deformation or defects in WS_2 structure is due to the sulfur deficit and can be classified as line defect [55,56].

3.6. Electrical Analysis

By examining the electrical properties of a thin film, defect states can be evaluated [55,57]. In this study, it has been revealed that carrier concentrations of as-deposited WS_2 films are quite high regardless of the gas flow rate variations, and all the films exhibit n-type semiconducting properties. Figure 13 represents the electrical properties of as-grown WS_2 thin film under different gas flow rates. The highest carrier concentration of 9.31×10^{19} cm^{-3} has been observed at 6 sccm gas flow with the resistivity of 2.01 Ω-cm. The highest carrier mobility of 2.42 cm^2/V.s with a carrier concentration of 3.58×10^{18} cm^{-3} have been found at 3 sccm of Ar flow rate. All the electrical properties of the film are given in Appendix A (Table A2).

In the case of semiconductor thin films, carrier concentration and mobility are considered two key factors that control the carrier transport properties. The carrier mobility is mainly affected by impurity scattering during high gas flow rate. It has been observed that carrier mobility decreases gradually with the increase in gas flow rate (Figure 13a). It is considered that the reduction in carrier mobility at a higher argon flow rate is due to an enhanced ionic impurity scattering, which also causes a great number of native defects. On the other hand, the resistivity and carrier concentration of the film gradually increases with the increase in gas flow rate (Figure 13b). The cause is that a higher argon flow rate increases the working pressure near the reaction zone. Consequently, the frequency of the collisions between the ionized atoms and the residual gas also increases. The higher resistivity of the WS_2 samples produced under the higher gas flow rate is, therefore, due to an increased ion dispersion effect caused by the greater number of native defects. [53,54,58,59]. Hence, a higher gas flow rate influences the yield rate of the sputtered atoms, which has an impact not only on film electrical properties but also on its structural defects. It is already reported that crystal defects have strong effects on the concentration and mobility of the films. Defect-free crystals provide higher carrier transportation property [60–62]. Thus, it can be concluded that the 5 sccm Ar gas flow rate effectively tailored the structural defects of WS_2 thin film to the least, which has been induced due to fabrication limitations. The above analysis clarifies that the film composition and gas flow rate have a crucial role in electronic film properties; certainly, that has a great impact on the performance of thin film solar cells.

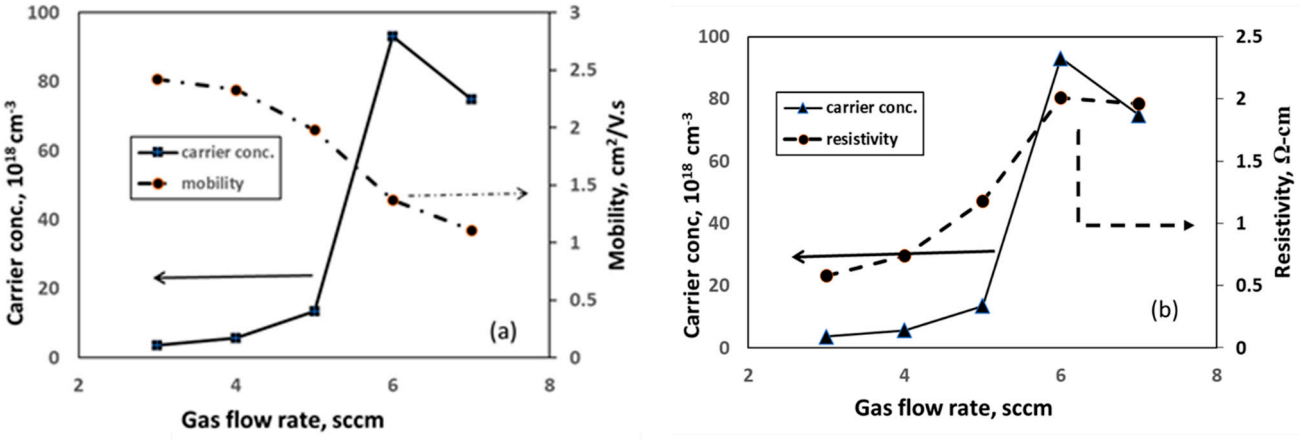

Figure 13. Electrical properties of as-grown WS_2 thin film under different Ar gas flow rates: (**a**) carrier concentration and mobility (**b**) carrier concentration and resistivity.

3.7. Evaluation of Solar Cell Performance

To validate and to pre-investigate the experimental findings, a Solar Cell Capacitance Simulator (SCAPS-1D) is used to oversee the performance of the proposed CdTe/WS_2 solar cell. A Solar Cell Capacitance Simulator (SCAPS) is a one-dimensional computer simulation software for simulating the alternating current and direct current electrical

attributes of thin film heterojunction solar cells. Although it was encouraged to study primarily CdTe and CIGS-based solar cells, SCAPS is currently used to investigate and validate the characteristics of all types of solar cells with different buffer layers as well. SCAPS-1D software essentially operates on two simple semiconductor equations, such as the Poisson equation and the continuity equation of electrons and holes in a steady state. In this paper, we have incorporated the experimental results of WS_2 as a buffer layer of CdTe/WS_2 solar cell and compare it with our previously reported literature. For illumination, a regular AM1.5 G spectrum (1000 W/m^2; T = 300 K) was used. Interface defect layers (IDL) of 10 nm thickness were used to assess the effect of defect densities subsisting on material interfaces. In addition, the neutral type of defect model is used in a simulation where the density of the defect in the active layer has been considered 10^{10} cm^{-3}. The thermal velocity of electrons and holes of 1×10^7 cm/s, the Gaussian energy distribution with a characteristic energy of 0.1 eV, have been considered for the model. The schematic structure of the simulated solar cell and the parameters used for this simulation are shown in the supplementary file in Figure S3, Tables S2 and S3, respectively. To evaluate and validate WS_2 as window layer material, initially, CdTe has been chosen as an absorber layer. The reasons for choosing CdTe are because of its availability in nature, comparatively low cost, commonly used in the industry, and most importantly, the matching in energy band. In this simulation, experimental data has been used to obtain the real scenario of the solar cell. Figure 14 shows the IV curve of WS_2-CdTe solar cell from SCAPS, and the inset shows QE% of the proposed device. From the simulation, it is revealed that WS_2-CdTe cell has exhibited V_{oc} of 1.04 V, J_{sc} of 26.94 mA/cm^2, FF of 85.39%, and efficiency of 23.99%. This result super passes our previous experimental findings (1.8% of efficiency) and encourages for commercialization of the device.

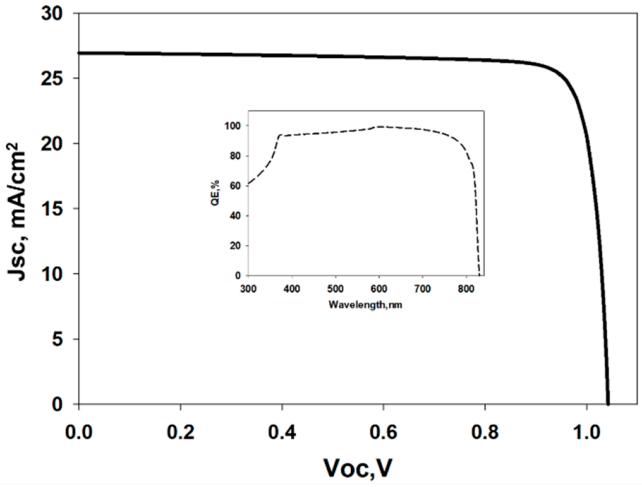

Figure 14. J-V curve of CdTe/WS_2 solar cell; QE% of CdTe/WS_2 solar cell at inset.

4. Conclusions

WS_2 films were deposited at different Ar gas flow rates by sputtering techniques. The deposited films possess a composite structure and exhibit peaks at (101) and (112) planes with a dominant orientation of the (101) plane. All the films are found at the 3R phase, which indicates the formation of a film with Bernal stacking order. The structural analysis reveals the formation of various degrees of defects at a higher gas flow rate, while the EDX analysis suggests that sulfur deficiency could be one of the reasons for the defects at a higher gas flow rate. However, 5 sccm Ar flow rate provides the largest crystallite size of 35.6 nm with the least dislocation density. FESEM images exhibit the presence of defects through visual inspection. All the films are found with non-uniform and porous microstructures. Spikes have also been observed in WS_2 crystallographic structure, which suggests the existence of native defects in WS_2 against different gas flow rates. From the

electrical analysis, it has been observed that whereas carrier concentration and resistivity of the film increase with the increase in Ar gas flow rate, carrier mobility decreases in this case. The highest carrier concentration of 9.31×10^{19} cm^{-3} has been found at 6 sccm Ar flow rate with the resistivity of 2.01 Ω-cm. The highest carrier mobility of 2.42 $cm^2/V.s$ has been detected at 3 sccm Ar flow rate with the carrier concentration of 3.58×10^{18} cm^{-3}. It indicates that carrier mobility is mainly affected by impurity scattering during high gas flow rate. The plasma state, therefore, aggravates at a higher gas flow rate and leads to an increased number of ion defects in the film. Hence, it can be said that tailoring of structural defects of WS_2 thin film is possible by the variation of Ar gas flow rate in the RF magnetron sputtering technique. Finally, taking the experimental data of fabricated WS_2 at 5 sccm Ar flow, a complete solar cell with a novel structure of FTO/ZnO/WS_2/CdTe/Ag has been simulated, and 23.99% conversion efficiency was achieved, which encourages the commercial fabrication of the proposed device.

Supplementary Materials: The following are available online at https://www.mdpi.com/article/10.3390/nano11071635/s1, Figure S1: FESEM images of WS_2, Figure S2: EDX data of WS_2 thin film under various Ar flow rate, Figure S3. Schematic of CdTe/WS_2 solar cell, Table S1: Thickness of WS_2 thin film, Table S2: Contact Material Properties, Table S3: Material Properties Used for simulation.

Author Contributions: Conceptualization, Methodology, M.A.; Revising draft preparation, Reviewing, K.S.B.R.; Methodology, Figure, G.M.; Concept—Reviewing, Editing, M.S.; Editing, M.A.I.; Project administration, K.S.; Funding acquisition, Supervision, N.A. All authors have read and agreed to the published version of the manuscript.

Funding: The authors would like to acknowledge the contribution of The National University of Malaysia through the research grant with code RS 2018-003. The authors also extend their appreciation to the King Saud University, Riyadh, Saudi Arabia, for their Researchers Supporting Project number RSP-2020/34.

Data Availability Statement: Data is available upon reasonable request from the corresponding author.

Acknowledgments: The authors would like to acknowledge the contribution of The National University of Malaysia through the research grant with code RS 2018-003. The authors also extend their appreciation to the King Saud University Riyadh, Saudi Arabia, for their Researchers Supporting Project number RSP-2021/34. The authors duly acknowledge the BOLD publication support (J510050002-BOLDRefresh2025) from iRMC, Universiti Tenaga Nasional, Malaysia.

Conflicts of Interest: The authors declare no conflict of interest.

Appendix A

Table A1. Geometric parameters obtained from as-grown WS_2 thin film XRD data.

Ar Flow Rate, Sccm	Angle, θ	FWHM, β	Scherrer Method	W-H Method		Dislocation Density δ, 10^{15} lines/m^2	Crystallite Per Unit Area N, 10^{15} m^{-2}
			Crystallite Size L, nm	Crystallite Size L, nm	Strain ε, 10^{-4}		
3	16.97	0.0233	35.3	19.5	27.3	26.29	20.46
4	17.14	0.0214	38.7	31.2	7.41	10.3	5.4
5	17.39	0.0217	44.8	35.6	2.36	0.78	3.74
6	17.44	0.0196	36.6	11.2	75.5	7.92	91.4
7	17.22	0.0196	42.6	11.8	71.2	7.13	64.5

Table A2. Electrical properties of the as-grown WS_2 thin film.

Ar Flow Rate, Sccm	Resistivity, Ω-cm	Mobility, $cm^2/V.s$	Carrier Concentration, cm^{-3}
3	0.58	2.42	3.58×10^{18}
4	0.74	2.33	5.64×10^{18}
5	1.18	1.98	5.05×10^{19}
6	2.01	1.37	9.31×10^{19}
7	1.96	1.11	7.48×10^{19}

References

1. Novoselov, K.; Jiang, D.; Schedin, F.; Booth, T.; Khotkevich, V.; Morozov, S.V.; Geim, A. Two-dimensional atomic crystals. *Proc. Natl. Acad. Sci. USA* **2005**, *102*, 10451–10453. [CrossRef] [PubMed]
2. Wang, Q.H.; Kalantar-Zadeh, K.; Kis, A.; Coleman, J.N.; Strano, M.S. Electronics and optoelectronics of two-dimensional transition metal dichalcogenides. *Nat. Nanotechnol.* **2012**, *7*, 699. [CrossRef] [PubMed]
3. Chowalla, M.; Shin, H.S.; Eda, G.; Li, L.J.; Loh, K.P.; Zhang, H. The chemistry of two-dimensional layered transition metal dichalcogenide nanosheets. *Nat. Chem.* **2013**, *5*, 263. [CrossRef] [PubMed]
4. Mak, K.F.; Lee, C.; Hone, J.; Shan, J.; Heinz, T.F. Atomically thin MoS_2: A new direct-gap semiconductor. *Phys. Rev. Lett.* **2010**, *105*, 136805. [CrossRef] [PubMed]
5. Splendiani, A.; Sun, L.; Zhang, Y.; Li, T.; Kim, J.; Chim, C.-Y.; Galli, G.; Wang, F. Emerging Photoluminescence in Monolayer MoS_2. *Nano Lett.* **2010**, *10*, 1271–1275. [CrossRef] [PubMed]
6. Jariwala, D.; Sangwan, V.K.; Lauhon, L.J.; Marks, T.J.; Hersam, M.C. Emerging device applications for semiconducting two-dimensional transition metal dichalcogenides. *ACS Nano* **2014**, *8*, 1102. [CrossRef] [PubMed]
7. Schmidt, H.; Giustiniano, F.; Eda, G. Electronic transport properties of transition metal dichalcogenide field-effect devices: Surface and interface effects. *Chem. Soc. Rev.* **2015**, *44*, 7715–7736. [CrossRef] [PubMed]
8. Zou, X.; Yakobson, B.I. An open canvas-2D materials with defects, disorder, and functionality. *Acc. Chem. Res.* **2015**, *48*, 73. [CrossRef] [PubMed]
9. Najmaei, S.; Yuan, J.; Zhang, J.; Ajayan, P.; Lou, J. Synthesis and Defect Investigation of Two-Dimensional Molybdenum Disulfide Atomic Layers. *Acc. Chem. Res.* **2014**, *48*, 31–40. [CrossRef]
10. Zatko, V.; Galbiati, M.; Dubois, S.M.-M.; Och, M.; Palczynski, P.; Mattevi, C.; Brus, P.; Bezencenet, O.; Martin, M.-B.; Servet, B.; et al. Band-Structure Spin-Filtering in Vertical Spin Valves Based on Chemical Vapor Deposited WS_2. *ACS Nano* **2019**, *13*, 14468–14476. [CrossRef]
11. Dickinson, R.G.; Pauling, L. The crystal structure of molybdenite. *J. Am. Chem. Soc.* **1923**, *45*, 1466–1471. [CrossRef]
12. Wyckoff, R.G.W. *Crystal Structures*; Interscience Publishers: New York, NY, USA, 1963; Volume 1.
13. Starnberg, H.I.; Brauer, H.E.; Hughes, H.P. *Electron Spectroscopies Applied to Low-Dimensional Materials*; Springer: Berlin/Heidelberg, Germany, 2001; Volume 41.
14. Tenne, R.; Margulis, L.; Genut, M.; Hodes, G. Polyhedral and cylindrical structures of tungsten disulphide. *Nat. Cell Biol.* **1992**, *360*, 444–446. [CrossRef]
15. Lorchat, E.; Froehlicher, G.; Berciaud, S. Splitting of Interlayer Shear Modes and Photon Energy Dependent Anisotropic Raman Response in N-Layer $ReSe_2$ and ReS_2. *ACS Nano* **2016**, *10*, 2752–2760. [CrossRef] [PubMed]
16. Hashimoto, A.; Suenaga, K.; Gloter, A.; Urita, K.; Iijima, S. Direct evidence for atomic defects in graphene layers. *Nat. Cell Biol.* **2004**, *430*, 870–873. [CrossRef] [PubMed]
17. Terrones, H.; Lv, R.; Terrones, M.; Dresselhaus, M.S. The role of defects and doping in 2D graphene sheets and 1D nanoribbons. *Rep. Prog. Phys.* **2012**, *75*, 062501. [CrossRef]
18. Zhao, P. *Understanding and Engineering Surface and Edge Defects of Transition Metal Dichalcogenides*; Technical Report No. UCB/EECS-2018-157; EECS Department, University of California: Berkeley, CA, USA, 2018.
19. Hanif, U.; Bernabé, M.; Luis, M.; Sánchez, R. Effect of defects on the performance of some photovoltaic solar cells: An introduction to research methods to engineering students. In Proceedings of the 44th SEFI Conference, Tampere, Finland, 12–15 September 2016.
20. Rafiq, M.K.S.B.; Amin, N.; Alharbi, H.F.; Luqman, M.; Ayob, A.; Alharthi, Y.S.; Alharthi, N.H.; Bais, B.; Akhtaruzzaman, M. WS_2: A New Window Layer Material for Solar Cell Application. *Sci. Rep.* **2020**, *10*, 771. [CrossRef] [PubMed]
21. Al-Mansoori, M.; Al-Shaibani, S.; Al-Jaeedi, A.; Lee, J.; Choi, D.; Hasoon, F.S. Effects of gas flow rate on the structure and elemental composition of tin oxide thin films deposited by RF sputtering. *AIP Adv.* **2017**, *7*, 125105. [CrossRef]
22. Vijaya, G.; Muralidhar, S.M.; Krupashankara, M.S.; Kulkarni, R.S. Effect of Argon Gas Flow Rate on the Optical and Mechanical Properties of Sputtered Tungsten Thin Film Coatings. *IOP Conf. Ser. Mater. Sci. Eng.* **2016**, *149*, 012075. [CrossRef]
23. Rafiq, M.K.S.B.; Ayoba, A.; Baisa, B.; Akhtaruzzamanb, M.; Aminc, N. Investigating the Impact of Growth Temperature on WS_2 Thin Film. *J. Kejuruter.* **2020**, *3*, 23–28.
24. Ahmadipour, M.; Arjmand, M.; Ain, M.F.; Ahmad, Z.A.; Pung, S.-Y. Effect of Ar:N_2 flow rate on morphology, optical and electrical properties of CCTO thin films deposited by RF magnetron sputtering. *Ceram. Int.* **2019**, *45*, 15077–15081. [CrossRef]

25. Kumar, M.; Mishra, S.; Mitra, R. Effect of Ar:N_2 ratio on structure and properties of Ni-TiN nanocomposite thin films pro-cessed by reactive RF/DC magnetron sputtering. *Surf. Coat. Technol.* **2013**, *228*, 100–114. [CrossRef]
26. Sundberg, J.; Lindblad, R.; Gorgoi, M.; Rensmo, H.; Jansson, U.; Lindblad, A. Understanding the effects of sputter damage in W–S thin films by HAXPES. *Appl. Surf. Sci.* **2014**, *305*, 2014. [CrossRef]
27. Tian, H.; Feng, L.P.; Liu, Z.T. Effect of N_2/Ar flow ratio on the structural and electrical properties of SrHfON thin films pre-pared by magnetron sputtering. *Vacuum* **2014**, *109*, 139–143. [CrossRef]
28. Vijayakumar, A.; Todi, R.M.; Sundaram, K.B. Effect of N_2/Ar Gas Mixture Composition on the Chemistry of SiCBN Thin Films Prepared by RF Reactive Sputtering. *J. Electrochem. Soc.* **2007**, *154*, H271–H274. [CrossRef]
29. Jiang, P.-C.; Chen, J.S.; Lin, Y.K. Structural and electrical characteristics of W–N thin films prepared by reactive rf sputtering. *J. Vac. Sci. Technol. A* **2003**, *21*, 616–622. [CrossRef]
30. Cheng, Y.; Zheng, Y.F. Effect of N_2/Ar gas flow ratio on the deposition of TiN/Ti coatings on NiTi shape memory alloy by PIIID. *Mater. Lett.* **2006**, *60*, 2243–2247. [CrossRef]
31. Wicher, B.; Chodun, R.; Nowakowska-Langier, K.; Trzcinski, M.; Skowroński, L.; Okrasa, S.; Minikayev, R.; Naparty, M.K.; Zdunek, K. Chemical and structural characterization of tungsten nitride (WNx) thin films synthesized via Gas Injection Mag-netron Sputtering technique. *Vacuum* **2019**, *165*, 266–273. [CrossRef]
32. Nossa, A.; Cavaleiro, A. Chemical and physical characterization of C(N)-doped W–S sputtered films. *J. Mater. Res.* **2004**, *19*, 2356–2365. [CrossRef]
33. Panich, N.; Wangyao, P.; Hannongbua, S.; Sricharoenchai, P.; Sun, Y. Effect of argon-nitrogen mixing gas during magnetron sputtering on titanium interlayer deposition with TiB_2 coatings on high speed steel. *Rev. Adv. Mater. Sci.* **2007**, *16*, 80–85.
34. Guruvenket, S.; Rao, G.M. Bias induced structural changes in tungsten nitride films deposited by unbalanced magnetron sputtering. *Mater. Sci. Eng. B* **2004**, *106*, 172–176. [CrossRef]
35. Addonizio, M.L.; Castaldo, A.; Antonaia, A.; Gambale, E.; Iemmo, L. Influence of process parameters on properties of reactively sputtered tungsten nitride thin films. *J. Vac. Sci. Technol. A* **2012**, *30*, 31506. [CrossRef]
36. Wilson, J.; Yoffe, A. The transition metal dichalcogenides discussion and interpretation of the observed optical, electrical and structural properties. *Adv. Phys.* **1969**, *18*, 193. [CrossRef]
37. Lin, Z.; Carvalho, B.R.; Kahn, E.; Lv, R.; Rao, R.; Terrones, H.; Pimenta, M.A.; Terrones, M. Defect engineering of two-dimensional transition metal dichalcogenides. *2D Mater.* **2016**, *3*, 022002. [CrossRef]
38. Tsay, C.-Y.; Cheng, H.-C.; Tung, Y.-T.; Tuan, W.-H.; Lin, C.-K. Effect of Sn-doped on microstructural and optical properties of ZnO thin films deposited by sol–gel method. *Thin Solid Film* **2008**, *517*, 1032–1036. [CrossRef]
39. Islam, M.A.; Hossain, M.; Aliyu, M.; Karim, M.; Razykov, T.; Sopian, K.; Amin, N. Effect of CdCl2 treatment on structural and electronic property of CdTe thin films deposited by magnetron sputtering. *Thin Solid Film* **2013**, *546*, 367–374. [CrossRef]
40. Stokes, A.R.; Wilson, A.J.C. The diffraction of X rays by distorted crystal aggregates—I. *Proc. Phys. Soc.* **1944**, *56*, 174. [CrossRef]
41. Balzar, D. X-Ray Diffraction Line Broadening: Modeling and Applications to High-Tc Superconductors. *J. Res. Natl. Inst. Stand. Technol.* **1993**, *98*, 321–353. [CrossRef] [PubMed]
42. Pijush, C.D.; Sarkar, S.; Das, R. X-ray diffraction study of the elastic properties of jagged spherical CdS nano-crystals. *Mater. Sci. Pol.* **2020**, *38*, 271–278.
43. Rabiei, M.; Palevicius, A.; Monshi, A.; Nasiri, S.; Vilkauskas, A.; Janusas, G. Comparing Methods for Calculating Nano Crystal Size of Natural Hydroxyapatite Using X-ray Diffraction. *Nanomaterials* **2020**, *10*, 1627. [CrossRef]
44. Beyerlein, K.R.; Snyder, R.L.; Li, M.; Scardi, P. Application of the Debye function to systems of crystallites. *Philos. Mag.* **2010**, 3891–3905. [CrossRef]
45. Kariper, İ.A. Structural, optical and porosity properties of CdI2 thin film. *J. Mater. Res. Technol.* **2016**, *5*, 77–83. [CrossRef]
46. Rawat, R.S.; Arun, P.; Vedeshwar, A.G.; Lee, P.; Lee, S. Effect of energetic ion irradiation on CdI2 films. *J. Appl. Phys.* **2004**, *95*, 7725–7730. [CrossRef]
47. Kariper, İ.A. Synthesis and characterization of cerium sulfide thin film. *Prog. Nat. Sci.* **2014**, *24*, 663–670. [CrossRef]
48. Munna, F.; Chelvanathan, P.; Sobayel, K.; Nurhafiza, K.; Sarkar, D.; Nour, M.; Sindi, H.; Rawa, M.; Sopian, K.; Amin, N.; et al. Effect of zinc doping on the optoelectronic properties of cadmium sulphide (CdS) thin films deposited by chemical bath deposition by utilising an alternative sulphur precursor. *Optik* **2020**, *218*, 165197. [CrossRef]
49. Kastl, C.; Koch, R.J.; Chen, C.T.; Eichhorn, J.; Ulstrup, S.; Bostwick, A.; Jozwiak, C.; Kuykendall, T.R.; Borys, N.J.; Toma, F.M.; et al. Effects of Defects on Band Structure and Excitons in WS_2 Revealed by Nanoscale Photoemission Spectroscopy. *ACS Nano* **2019**, *13*, 1284–1291. [CrossRef] [PubMed]
50. Regula, M.; Ballif, C.; Moser, J.; Lévy, F. Structural, chemical, and electrical characterisation of reactively sputtered WSx thin films. *Thin Solid Film* **1996**, *280*, 67–75. [CrossRef]
51. Islam, M.A.; Rahman, K.S.; Sobayel, K.; Enam, T.; Ali, A.M.; Zaman, M.; Akhtaruzzaman, M.; Amin, N. Fabrication of high efficiency sputtered CdS: O/CdTe thin film solar cells from window/absorber layer growth optimization in magnetron sputtering. *Sol. Energy Mater.* **2017**, *172*, 384–393. [CrossRef]
52. Moser, J.; Lévy, F. Random stacking in MoS_{2-x} sputtered thin films. *Thin Solid Film* **1994**, *240*, 56–59. [CrossRef]
53. Tseng, K.-S.; Lo, Y.-L. Effect of sputtering parameters on optical and electrical properties of ITO films on PET substrates. *Appl. Surf. Sci.* **2013**, *285*, 157–166. [CrossRef]

54. Jung, Y.S. Spectroscopic ellipsometry studies on the optical constants of indium tin oxide films deposited under various sputtering conditions. *Thin Solid Film* **2004**, *467*, 36–42. [CrossRef]
55. Liu, Z.; Suenaga, K.; Wang, Z.; Shi, Z.; Okunishi, E.; Iijima, S. Identification of active atomic defects in a monolayered tungsten disulphide nanoribbon. *Nat. Commun.* **2011**, *2*, 213. [CrossRef]
56. Komsa, H.-P.; Kurasch, S.; Lehtinen, O.; Kaiser, U.; Krasheninnikov, A.V. From point to extended defects in two-dimensional MoS_2: Evolution of atomic structure under electron irradiation. *Phys. Rev. B* **2013**, *88*, 035301. [CrossRef]
57. Han, Y.; Hu, T.; Li, R.; Zhou, J.; Dong, J. Stabilities and electronic properties of monolayer MoS_2 with one or two sulfur line vacancy defects. *Phys. Chem. Chem. Phys.* **2014**, *17*, 3813–3819. [CrossRef] [PubMed]
58. Rogozin, A.I.; Vinnichenko, M.V.; Kolitsch, A.; Moller, W. Effect of deposition parameters on properties of ITO films prepared by reactive middle frequency pulsed dual magnetron sputtering. *J. Vac. Sci. Technol.* **2004**, *22*, 349–355. [CrossRef]
59. Shin, D.-H.; Kim, Y.-H.; Han, J.-W.; Moon, K.-M.; Murakami, R.-I. Effect of process parameters on electrical, optical properties of IZO films produced by inclination opposite target type DC magnetron sputtering. *Trans. Nonferrous Met. Soc. China* **2009**, *19*, 997–1000. [CrossRef]
60. Dominguez, J.E.; Fu, L.; Pan, X.Q. Effect of crystal defects on the electrical properties in epitaxial tin dioxide thin films. *Appl. Phys. Lett.* **2002**, *81*, 5168–5170. [CrossRef]
61. Cheng, L.-C.; Wu, M.-R.; Huang, C.-Y.; Juang, T.-K.; Liu, P.-L.; Horng, R.H. Effect of Defects on the Properties of $ZnGa_2O_4$ Thin-Film Transistors. *ACS Appl. Electron. Mater.* **2019**, *1*, 253–259. [CrossRef]
62. Scharpf, J.; Denisenko, A.; Pietzka, C.; Kohn, E. Effect of surface defects by RF oxygen plasma on the electrical properties of thin boron-doped diamond layers in electrolyte. *Diam. Relat. Mater.* **2011**, *20*, 1250–1254. [CrossRef]